



HAL
open science

Dynamics of dense granular flows of small-and-large-grain mixtures in an ambient fluid

C. Meruane, A. Tamburrino, Olivier Roche

► **To cite this version:**

C. Meruane, A. Tamburrino, Olivier Roche. Dynamics of dense granular flows of small-and-large-grain mixtures in an ambient fluid. *Physical Review E: Statistical, Nonlinear, and Soft Matter Physics*, 2012, 86, pp.026311. 10.1103/PhysRevE.86.026311 . hal-00784192

HAL Id: hal-00784192

<https://hal.science/hal-00784192>

Submitted on 10 Mar 2022

HAL is a multi-disciplinary open access archive for the deposit and dissemination of scientific research documents, whether they are published or not. The documents may come from teaching and research institutions in France or abroad, or from public or private research centers.

L'archive ouverte pluridisciplinaire **HAL**, est destinée au dépôt et à la diffusion de documents scientifiques de niveau recherche, publiés ou non, émanant des établissements d'enseignement et de recherche français ou étrangers, des laboratoires publics ou privés.

Dynamics of dense granular flows of small-and-large-grain mixtures in an ambient fluid

C. Meruane* and A. Tamburrino

Departamento de Ingeniería Civil, Universidad de Chile Blanco Encalada 2002, Casilla 228-3, Santiago, Chile

O. Roche

*Clermont Université, Université Blaise Pascal, Laboratoire Magmas et Volcans, BP 10448, F-63000 Clermont-Ferrand, France;**CNRS, UMR 6524; LMV, F-63038 Clermont-Ferrand, France; IRD, R 163, LMV, F-63038 Clermont-Ferrand, France*

(Received 1 March 2012; published 20 August 2012)

Dense grain flows in nature consist of a mixture of solid constituents that are immersed in an ambient fluid. In order to obtain a good representation of these flows, the interaction mechanisms between the different constituents of the mixture should be considered. In this article, we study the dynamics of a dense granular flow composed of a binary mixture of small and large grains immersed in an ambient fluid. In this context, we extend the two-phase approach proposed by Meruane *et al.* [*J. Fluid Mech.* **648**, 381 (2010)] to the case of flowing dense binary mixtures of solid particles, by including in the momentum equations a constitutive relation that describes the interaction mechanisms between the solid constituents in a dense regime. These coupled equations are solved numerically and validated by comparing the numerical results with experimental measurements of the front speed of gravitational granular flows resulting from the collapse, in ambient air or water, of two-dimensional granular columns that consisted of mixtures of small and large spherical particles of equal mass density. Our results suggest that the model equations include the essential features that describe the dynamics of grains flows of binary mixtures in an ambient fluid. In particular, it is shown that segregation of small and large grains can increase the front speed because of the volumetric expansion of the flow. This increase in flow speed is damped by the interaction forces with the ambient fluid, and this behavior is more pronounced in water than in air.

DOI: [10.1103/PhysRevE.86.026311](https://doi.org/10.1103/PhysRevE.86.026311)

PACS number(s): 45.70.Mg, 45.70.Ht, 81.05.Rm

I. INTRODUCTION

Most dense grain flows in nature, such as debris avalanches, pyroclastic flows, landslides, and submarine avalanches, involve solid particles having a wide range of sizes and that are immersed in an ambient fluid [1]. The influence of the interactions among the solid constituents on the dynamics of these dense heterogeneous flows has not been studied extensively yet [2,3], and a better understanding of this issue is required to improve the representation of these natural phenomena [4].

Granular flows of binary mixtures often exhibit a nonuniform spatial distribution of particles owing to the nature of the flow and the properties of their constituents [5,6]. For instance, dry granular avalanches of small and large grains are very efficient at sorting particles by size as the small particles commonly percolate downward and the large ones rise up to the free surface of the flow [5,6]. This segregation mechanism may compete against the diffusive remixing mechanism that occurs in rapid avalanches [7–9], or against the mass effect mechanism in the case of large grain size ratios as large grains sink toward the bottom because of their greater mass [10]. Moreover, when the large particles have a higher internal friction coefficient than the small ones, segregation causes fingering instability of the avalanche front [11] or spontaneous stratification in two-dimensional silos [12]. Furthermore, the interactions between the particles and their ambient fluid may also have an influence on the mixture flow dynamics, as shown

for homogeneous granular flows [13]. In water, front fingering instability and inverse vertical segregation are damped in binary mixtures of small and large particles [14,15]. In air, spontaneous segregation caused by vertical vibration may occur in binary mixtures of particles of equal size but different density as a consequence of an internal air flow [16,17].

Another notable feature of granular flows of binary mixtures is their high mobility, commonly defined as the ratio between the runout distance to the fall height, compared to cases involving only one grain size. This difference has been reported in laboratory experiments [18,19] and in soft particle discrete element numerical simulations [20], and it was established that this high mobility reaches a maximum for small grains fractions of about 30% [18]. This increase in mobility has been attributed to a thin layer of small grains at the flow base formed by percolation, which changes from sliding to rolling the frictional dynamics at the base of the granular flow [19,20]; however, this hypothesis is not able to explain the high mobility of granular avalanches in nature where the flows occur over rough terrains, so that the physical origin of the high mobility of natural granular flows remains controversial [21].

The examples described above show that in order to obtain a good representation of dense granular flows of binary mixtures, the solid-solid and solid-fluid interaction mechanisms between the different constituents of the mixture should be considered. In this context, the mixture theory is a useful tool for describing the dynamics of these flows [22,23]. This concept was addressed recently by Refs. [8,24,25], where the mixture theory was used to describe particle-size segregation and diffusive remixing in granular avalanches of two or three constituents. These models consist of a single equation for the volume fraction of the smaller particles, and are closely related to the models proposed by Refs. [5,7]. Although these

*cmeruane@ing.uchile.cl; Also at Laboratoire Magmas et Volcans, UMR Université Blaise Pascal, 5 rue Kessler, 63038 Clermont-Ferrand, France.

approaches are promising for predicting segregation in dense granular avalanches, they do not include empirical relations that account for the segregation and remixing fluxes as well as their dependence with the particles and flow properties [8]. In particular, these models do not consider the feedback that exists between the particle-size distribution and the dynamics of the flow [26]. In this context, [13] recently used the mixture theory to develop a conceptual model for representing compressible monodisperse granular flows of solid particles in an ambient fluid, in which the dynamics of each phase was solved separately. As this two-phase approach is based on the mixture theory, it can be extended to the case of two solid constituents by including the corresponding constitutive relation that describes the interactions between the solid components. An advantage of extending this model is that the feedback between the spatial variations of the volume fractions of the solids and the dynamics of the mixture arises as a natural consequence of the approach.

The aim of the present work is to study the dynamics of a dense granular flow composed of a binary mixture of small and large grains and immersed in an ambient fluid. In this context, we extend the two-phase approach proposed by Ref. [13] to the case of binary mixtures, by including in the momentum equations a constitutive relation that describes the interaction mechanisms between the solids constituents in a dense regime. Although the governing equations are general for any binary mixture of solid constituents in a dense regime, we focus on mixtures of small and large spherical particles of equal mass density and surface roughness. For this case, the dynamics of the granular flow is analyzed experimentally and numerically for the collapse and spreading of two-dimensional granular columns in air or water, for different grain size ratios of the solid particles and column height-to-length ratios.

This article is organized as follows. In Sec. II the derivation of the governing equations is detailed. The experimental and numerical methods for the collapse and spreading of a two-dimensional granular column are described in Sec. III. The results are presented in Sec. IV, in which the model equations are validated by comparing directly the numerical results with the experimental measurements using the front speed to describe the flow. Finally, in Sec. V we discuss the results and show that segregation of the granular flow increases the front speed, which is damped by the ambient fluid effects that in turn decreases the speed of the grains.

II. GOVERNING EQUATIONS

A. Three-phase framework

The two-phase approach proposed by Ref. [13] is extended here to obtain the governing equations for a dense granular flow consisting of binary mixtures of small and large grains and immerse in an ambient fluid.

In order to identify the components of the mixture, the subindex $\alpha = 0$ is defined for the fluid phase and $\alpha = 1, 2$ are defined for the solid components, with $\alpha = 1$ denoting small grains and $\alpha = 2$ denoting large grains. The mixture occupies a reference volume V , which is large compared to the particles size, and the constituent α occupies a volume V_α within V such as $V = \sum_\alpha V_\alpha$. Each constituent has a material density γ_α , a

velocity $u_{\alpha i}$, and a volumetric concentration c_α . The partial density is defined as $\rho_\alpha \equiv c_\alpha \gamma_\alpha$.

The mass and momentum conservation equations for each constituent in a dense regime can be written as [13]

$$\begin{aligned} \frac{\partial \rho_\alpha}{\partial t} + \frac{\partial(\rho_\alpha u_{\alpha i})}{\partial x_i} &= 0, \quad \alpha = 0, 1, 2, \quad (1) \\ \frac{\partial \rho_0 u_{0i}}{\partial t} + \frac{\partial(\rho_0 u_{0j} u_{0i})}{\partial x_j} &= \rho_0 g_i + \frac{\partial}{\partial x_j} \left[(\mu_0 + \mu_T) \left(\frac{\partial u_{0i}}{\partial x_j} + \frac{\partial u_{0j}}{\partial x_i} \right) \right] - c_0 \frac{\partial p_0}{\partial x_i} \\ &\quad - \sum_{\beta=1}^2 K_\beta (u_{0i} - u_{\beta i}), \quad (2) \\ \frac{\partial \rho_\alpha u_{\alpha i}}{\partial t} + \frac{\partial(\rho_\alpha u_{\alpha j} u_{\alpha i})}{\partial x_j} &= \rho_\alpha g_i - \frac{\partial p_\alpha}{\partial x_i} + s_{ij} \frac{\partial p_\alpha}{\partial x_j} \tan \varphi_\alpha - c_\alpha \frac{\partial p_0}{\partial x_i} \\ &\quad + K_\alpha (u_{0i} - u_{\alpha i}) + \hat{m}_{\alpha\beta i}, \quad \alpha \neq \beta = 1, 2, \quad (3) \end{aligned}$$

where x_i correspond to the i th direction; p_α is the pressure of the constituent α ; φ_α is the internal friction angle of the solid constituent α and $s_{\alpha ij} \equiv \text{sgn}(\partial u_{\alpha i} / \partial x_j)$; K_α is a well constrained phenomenological drag function [27] that is described in detail in Ref. [13]; μ_0 and μ_T are the dynamic and turbulent viscosity of the fluid phase, with μ_T obtained from a standard turbulence energy-dissipation model ($k - \epsilon$ model [28]), which includes the work done by the fluid drag force as a production term in both k and ϵ equations [29], and it is presented in detail in Ref. [13]; finally, $\hat{m}_{\alpha\beta i} = -\hat{m}_{\beta\alpha i}$ represents the reciprocal forces between the solid components in a dense regime, whose representation is the focus of this article.

The system of equations (1)–(3) is closed with the saturation constraint $\sum_{\alpha=0}^2 c_\alpha = 1$ and with the solid pressure closure proposed by Ref. [13]. In this closure, the solid pressure is defined as the reaction force that arises in response to the constraint of incompressibility when the solid particles are packed, which in the static case can be interpreted as the fraction of the weight of the solids that is sustained by direct contacts among solid particles or at boundaries. Here we extend that definition and interpret the solid pressure of the constituent α as the reaction force related to the constraint of incompressibility when the particles of the solid constituent α are packed, which can be mathematically represented by

$$p_\alpha = \begin{cases} p_\alpha & c_\alpha \geq c_\alpha^*, \\ 0 & c_\alpha < c_\alpha^*, \end{cases} \quad \alpha = 1, 2, \quad (4)$$

where c_α^* is the loose packing concentration of the solid constituent α , which depends on the relative particle diameter and concentration of the solid constituents of the mixture, as discussed later in this section.

Note that the collisional stresses are not considered in Eq. (3) as [13] showed that these can be neglected for dense granular flows at the laboratory scale considered. Nevertheless, the rate-dependent collisional part for the dilute and intermediate regimes may be included in future works, and the kinetic theory may help to investigate this issue [30,31].

B. Constitutive relation for the interaction force between solid constituents in a dense regime

As demonstrated in the Appendix, the interaction force between the solid components $\hat{m}_{\alpha\beta i} = -\hat{m}_{\beta\alpha i}$ can be mathematically expressed as

$$\hat{m}_{\beta\alpha i} = -\hat{m}_{\alpha\beta i} = c_\alpha \frac{\partial \hat{T}_{\alpha ij}^\beta}{\partial x_j} - c_\beta \frac{\partial \hat{T}_{\beta ij}^\alpha}{\partial x_j}. \quad (5)$$

where $\hat{T}_{\alpha ij}^\beta$ represents the tensor of superficial forces acting on the surface of the constituent α due to the other solid component β . In this section, we derive the constitutive relation for this tensor of superficial forces.

First, let us concentrate on the first component of Eq. (5) $c_\alpha \partial \hat{T}_{\alpha ij}^\beta / \partial x_j$, which represents the action force of β on α . Defining $\hat{T}_{\alpha ij}^\beta$ as the sum of a compression part $-\hat{p}_\alpha^\beta$, and a shear stress part $\hat{\tau}_{\alpha ij}^\beta$, so that $\hat{T}_{\alpha ij}^\beta = -\hat{p}_\alpha^\beta \delta_{ij} + \hat{\tau}_{\alpha ij}^\beta$, this term is written as

$$c_\alpha \frac{\partial \hat{T}_{\alpha ij}^\beta}{\partial x_j} = -c_\alpha \frac{\partial \hat{p}_\alpha^\beta}{\partial x_i} + c_\alpha \frac{\partial \hat{\tau}_{\alpha ij}^\beta}{\partial x_j}. \quad (6)$$

In Eq. (6), the normal interaction term $-c_\alpha \partial \hat{p}_\alpha^\beta / \partial x_i$ can be interpreted as a buoyancy force, as it represents the normal force exerted by the constituent β on the surface of the constituent α , so that \hat{p}_α^β is the pressure of the constituent β , i.e., $\hat{p}_\alpha^\beta = p_\beta$. The shear interaction term of Eq. (6), $c_\alpha \partial \hat{\tau}_{\alpha ij}^\beta / \partial x_j$, on the other hand, represents the tangential force exerted by the constituent β on the surface of the constituent α , so that by analogy to the homogeneous dense flow regime, the shear stress component $\hat{\tau}_{\alpha ij}^\beta$ can be represented by the Mohr-Coulomb condition with an isotropic solid pressure assumption, which states that the compressive and shear stresses acting in a particular plane over a particular point are related by (e.g., [32])

$$|\hat{\tau}_{\alpha ij}^\beta| = (1 - \delta_{ij}) |\hat{p}_\alpha^\beta| \tan \varphi_\alpha^\beta = (1 - \delta_{ij}) |p_\beta| \tan \varphi_\alpha^\beta, \quad (7)$$

where φ_α^β represents the friction angle between the constituents β and α . Note that we have assumed isotropic solid pressure, which means that for the dynamic case the ratio between the shear to normal stresses is the same along any plane. This assumption is justified by the fact that granular flows behave more like a fluid than a solid, as shown by several works that considered the isotropic assumption (e.g., [33–36]).

Finally, the action force of the constituent β on α in a dense regime is represented by

$$c_\alpha \frac{\partial \hat{T}_{\alpha ij}^\beta}{\partial x_j} = -c_\alpha \frac{\partial p_\beta}{\partial x_i} - s_{\alpha ij}^\beta c_\alpha \frac{\partial p_\beta}{\partial x_j} \tan \varphi_\alpha^\beta, \quad (8)$$

with $s_{\alpha ij}^\beta \equiv \text{sgn}[(u_{\beta i} - u_{\alpha i}) / \partial x_j]$, which ensures that the tangential force exerted by the constituent β on α is opposite to the movement of α ; therefore, it transfers momentum from α to β .

In the same way, the second component of Eq. (5), $-c_\beta \partial \hat{T}_{\beta ij}^\alpha / \partial x_j$, which represents the reaction force of the constituent β on α due to the action force of α on β , is

represented by

$$-c_\beta \frac{\partial \hat{T}_{\beta ij}^\alpha}{\partial x_j} = c_\beta \frac{\partial p_\alpha}{\partial x_i} + s_{\beta ij}^\alpha c_\beta \frac{\partial p_\alpha}{\partial x_j} \tan \varphi_\beta^\alpha. \quad (9)$$

Hence, the reciprocal interaction force between the solid components has the form of a multicomponent Mohr-Coulomb yield criterion with an isotropic solid pressure assumption, due to

$$\begin{aligned} \hat{m}_{\beta\alpha i} &= -\hat{m}_{\alpha\beta i} \\ &= -c_\alpha \frac{\partial p_\beta}{\partial x_i} - s_{\alpha ij}^\beta c_\alpha \frac{\partial p_\beta}{\partial x_j} \tan \varphi_\alpha^\beta + c_\beta \frac{\partial p_\alpha}{\partial x_i} \\ &\quad + s_{\beta ij}^\alpha c_\beta \frac{\partial p_\alpha}{\partial x_j} \tan \varphi_\beta^\alpha, \end{aligned} \quad (10)$$

where $s_{\alpha ij}^\beta = -s_{\beta ij}^\alpha$ and $\varphi_\alpha^\beta = \varphi_\beta^\alpha$.

C. Packing concentration, solid pressure, and percolation of small grains

For obtaining the pressure of each solid component in the solid pressure closure (4), the loose packing concentration of each solid constituent c_α^* has to be determined. For doing this, we present a function for the loose packing concentration of the mixture c^* , which is a general relation that allows us to determine c_α^* . Then, we analyze two mechanisms that generate percolation of small grains: the kinetic sieving mechanism and the sifting of small grains. The way for representing these two mechanisms is by modifying the representation of the packing limits of the two species in the solid pressure equation (4), which is discussed below.

Regarding the loose packing concentration of the mixture c^* , it is well known that mixtures of small and large grains can pack to higher concentrations than assemblages of monosized particles, and the improvement on the packing concentration depends on the size ratio d_1/d_2 , and on the fractional solid concentration of each constituent $X_\alpha = c_\alpha / (c_1 + c_2)$, $\alpha = 1, 2$ (pp. 135–163 of Ref. [37]). Several models account for the influence of these parameters on the mixture packing (pp. 135–163 of Ref. [37]), and we chose the empirical formula of Ref. [38], which for bimodal spheres of the same composition and packing concentration can be written as

$$\begin{aligned} c^*(d_1/d_2, X_2) &= \begin{cases} (1 - \sqrt{d_1/d_2})c(1-c)(2-c)X_2 + c & X_2 \leq 1/(2-c), \\ (1 - \sqrt{d_1/d_2})c(2-c)(1-X_2) + c & X_2 > 1/(2-c), \end{cases} \\ & \quad (11) \end{aligned}$$

where c is the loose packing concentration of monosized particles that is equal to about 0.6 for spheres (e.g., [13,39]). Equation (11) indicates that when both constituents of spherical particles have the same size, i.e., $d_1/d_2 = 1$, the loose packing concentration of the mixture is equal to the loose packing concentration of monosized particles, i.e., $c^* = c$. On the contrary, if the spherical particles have different sizes, the loose packing concentration of the mixture is greater than the packing concentration of monosized particles, i.e., $c^* > c$. In this case, the packing concentration is strongly dependent on the relative concentration of small grains. An example of this dependence is shown in Fig. 1, where optimal packing occurs

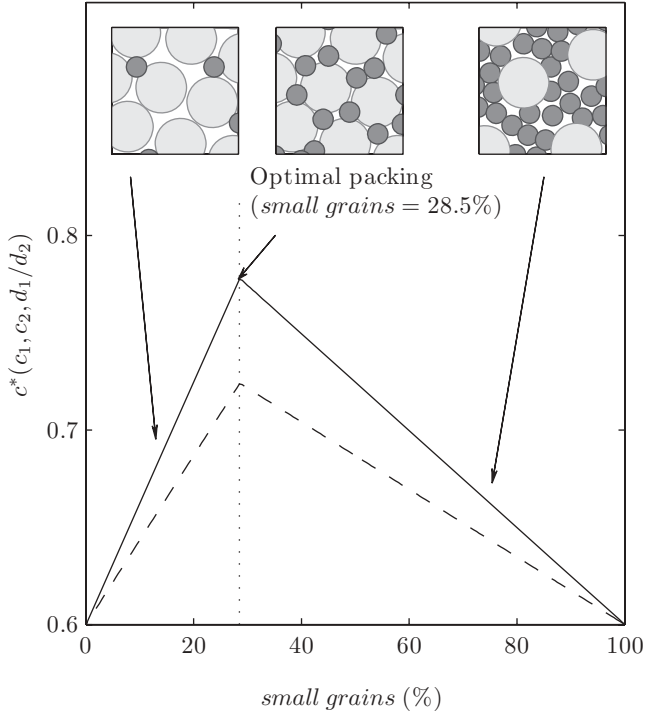


FIG. 1. Calculated loose packing concentration of binary mixtures of small and large grains using (11) and $c = 0.6$, $d_1/d_2 = 0.067$ (solid line), and $d_1/d_2 = 0.233$ (dashed line). Adapted from Ref. [37].

at $\sim 28\%$ of small grains, when small grains fill optimally the voids of the large spheres network (p. 140 of Ref. [37]).

Furthermore, the loose packing concentration of one solid component can be calculated by considering that $c^* = c_1^* + c_2^*$; therefore, when the mixture is packed, the space left by one solid component in the mixture packing is the loose packing limit of the other solid component, which can be written as

$$c_\alpha^* = c^* - c_\beta, \quad \alpha \neq \beta = 1, 2. \quad (12)$$

The inclusion of the loose packing limits of Eq. (12) in the solid pressure closure (4) means that for mixture concentrations less than c^* both small and large particles lose their contacts and fall down, if there are no other forces that can support their weight. However, it is well known that below a critical value of the mixture concentration, only the small particles fall down while the large particles remain packed [5]. This percolation of small grains is due to the kinetic sieving mechanism, which is explained by the fact that once the mixture is in motion and consequently expands, small grains have a greater probability than the large ones of finding a hole in which they can fall into Ref. [5]. This means that there is a critical value of the mixture concentration, smaller than c^* , for which only small grains fall down while the large particles remain packed.

The way for representing the kinetic sieving of small grains is by modifying the packing limits of small and large grains, particularly by decreasing the packing limit of the large grains; therefore, we make two assumptions: first, c^* is the limit under which (i.e., $c_1 + c_2 < c^*$) the small particles percolate downward while the large particles remain packed; and second, ηc^* is the limit under which (i.e., $c_1 + c_2 < \eta c^*$) both large and small particles fall down, with $\eta \leq 1$ an empirical parameter.

In other words, once the mixture expands, there is an interval for the mixture concentration ($\eta c^* < c_1 + c_2 < c^*$) for which small grains percolate between the large ones. In this way, for including percolation of small grains, the loose packing concentration used in the pressure closure (4) for small and large particles is represented by

$$c_1^* = c^* - c_2, \quad c_2^* = \eta c^* - c_1. \quad (13)$$

The empirical function η has to preserve the physical limit of $\eta = 1$ when $c_1 = 0$ or $c_2 = 0$ or $d_1 = d_2$ (one of the two species is absent or they have the same size), and it should increase with d_1/d_2 as percolation is more likely to occur for small values of d_1/d_2 . Based on this, we propose the following expression:

$$\eta(c_1, c_2, d_1/d_2) = \exp(-\sigma c_1 c_2 [1 - d_1/d_2]), \quad (14)$$

with σ the kinetic sieving coefficient, which is an empirical constant order 1 that is discussed in the results section.

Another mechanism that produces the percolation of small grains is the sifting of small grains, which occurs when $d_1/d_2 < (2/\sqrt{3} - 1) \approx 0.15$ that corresponds to the Apollonian ratio for which a small particle exactly fits inside a hole between three tangent spheres in the network of the larger particles [40]. This means that when $d_1/d_2 < 0.15$ and the large particles are in point contact with one another, i.e., $c_2 \geq c$, percolation of small particles occurs spontaneously as long as the interstitial voids between the large particles are not filled. In the context of the pressure closure (4) and the mixture packing limit (11), this means that $c_1^* = (1 - \sqrt{d_1/d_2})c(1 - c)$ if $c_2 \geq c$.

D. Dimensionless variables for the granular dam-break problem

We use the governing equations for studying the collapse and spreading of two-dimensional granular columns in air or water (i.e., the granular dam-break problem), for different binary mixtures of small and large spherical particles of equal mass density and surface roughness (i.e., $\gamma_1 = \gamma_2$ and $\varphi_1^2 = \varphi_2 = \varphi$). The characteristics scales for this particular problem were derived by Ref. [13] and are as follows: the characteristic time scale $T = \sqrt{h_o/g'}$, where $g' = g(\gamma_\alpha - \gamma_o)/\gamma_\alpha$ is the reduced gravity and h_o is the initial column height; the characteristic horizontal and vertical velocity scale $U = V = \sqrt{g'h_o}$; and the characteristic horizontal and vertical length scale $L = H \sim UT \sim h_o$. Using the loose packing density of the mixture $c^*\gamma_\alpha$, and the material density of the fluid γ_o , as density scales, then the following dimensionless variables are obtained:

$$\begin{aligned} \tilde{t} &= t \sqrt{\frac{g'}{h_o}}, & \tilde{x}_i &= \frac{x_i}{h_o}, & \tilde{u}_{ai} &= \frac{u_{ai}}{\sqrt{g'h_o}}, \\ \tilde{p}_0 &= \frac{p_0}{\gamma_o g' h_o}, & \tilde{p}_\alpha &= \frac{p_\alpha}{c^* \gamma_1 g' h_o} & \alpha &= 1, 2, \end{aligned} \quad (15)$$

where $x_1 = x$, $x_2 = y$ are the horizontal and vertical directions, respectively, and \sim denotes scaled variables.

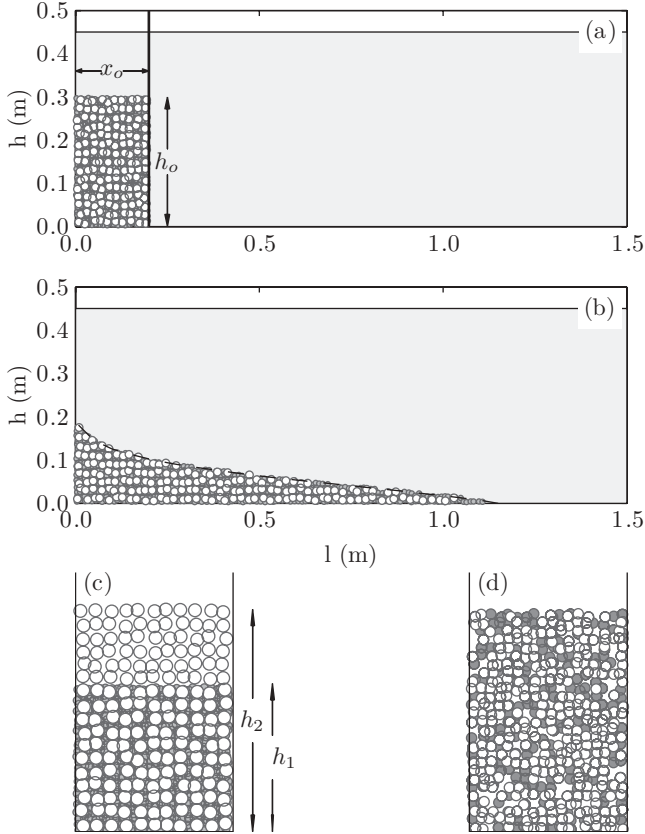


FIG. 2. (a) Sketch of the experimental setup: a perspex rectangular channel of 1.5 m long, 0.5 m deep, and 0.1 m wide, with an initial column of grains of aspect ratio h_o/x_o . (b) Sketch of the final deposit in water. (c) Sketch of the initial column of grains for mixtures A ($d_1/d_2 = 0.067$) listed in Table II, with h_1 and h_2 the column height of small and large grains, respectively. (d) Sketch of the initial column of grains for mixtures B ($d_1/d_2 = 0.233$) listed in Table II.

III. METHODS

A. Experimental procedure

Experiments were conducted in a 1.5-m-long perspex rectangular channel, 0.5 m deep and 0.1 m wide, by suddenly opening a vertical sluice gate that initially hold a granular column of glass beads (with $\varphi = 26^\circ$) in air or water, as sketched in Fig. 2(a) (the water depth was 0.45 m). We used glass beads because they are denser than the ambient fluids and their subspherical shape makes comparison between experiments and numerical results easier. The initial column aspect ratio h_o/x_o (with x_o the initial reservoir length) was in the range 2–8, with $x_o = 0.1$ m for $h_o/x_o = \{2,3,4\}$ and $x_o = 0.05$ m for $h_o/x_o = \{6,8\}$. For each aspect ratio, we used two types of binary mixtures of small and large glass beads ($d_1 = 0.2$ mm and $d_2 = 3.0$ mm, $d_1 = 0.7$ mm and $d_2 = 3.0$ mm), which led to a total of four sets of experiments listed in Table I. It is important to mention that each sample of particles of diameter 0.2, 0.7, and 3.0 mm was slightly polydisperse and well sorted. The actual grain size ranges were 0.125–0.250 mm for particles of 0.2 mm, 0.6–0.8 mm for particles of 0.7 mm, and 2.8–3.2 mm for particles of 3 mm.

TABLE I. Laboratory and numerical experiments of binary mixtures in air and water, with d_1 and d_2 the diameter of small and large grains, and v_0 the kinematic viscosity of the fluid phase. For each set, $\gamma_1 = \gamma_2 = 2.5 \times 10^3$ kg m $^{-3}$, $\varphi_1 = \varphi_2 = 26^\circ$, $c = 0.6$, $x_o = 0.1$ m for $h_o/x_o = \{2,3,4\}$, and $x_o = 0.05$ m for $h_o/x_o = \{6,8\}$, $\Delta x = \Delta y = 7.14 \times 10^{-3}$ m, and $\Delta t = 2.5 \times 10^{-3}$ s.

| Set | (d_1, d_2) ($\times 10^{-3}$ m) | d_1/d_2 | γ_0 (kg m $^{-3}$) | v_0 ($\times 10^{-5}$ m 2 s $^{-1}$) |
|---------------|---------------------------------------|-----------|-------------------------------|--|
| A1 (in air) | (0.2, 3.0) | 0.067 | 1.2 | 1.7 |
| B1 (in air) | (0.7, 3.0) | 0.233 | 1.2 | 1.7 |
| A2 (in water) | (0.2, 3.0) | 0.067 | 1000 | 0.1 |
| B2 (in water) | (0.7, 3.0) | 0.233 | 1000 | 0.1 |

Each set of experiments was carried out by varying the proportion of small and large glass beads. In the case of mixtures with $d_1/d_2 \geq 0.15$ (sets B1 and B2 in Table I) we used homogeneous mixtures with four initial relative solid concentrations of small particles equal to 0, 25, 50, and 100%. The homogeneity of the mixture was achieved by adding small volumes of material into the reservoir as the ambient fluid was present inside the channel as shown in Fig. 2(a). In contrast, for mixtures with $d_1/d_2 < 0.15$ (sets A1 and A2 in Table I), for which percolation of small particles between the voids of large particles occurred spontaneously, different proportions of small and large particles were achieved by varying the height of the column of large particles [h_2 in Table II and Fig. 2(c)], and filling at different levels [h_1 in Table II and Fig. 2(c)] the interstices between them (without forcing the large particles apart).

The experimental procedure can be summarized as follows. The glass beads were placed into the reservoir without agitation or vibration. The channel was illuminated with diffuse back lighting that provided a good contrast for video analysis, and a video camera was carefully aligned along the horizontal direction. The sluice gate was then manually removed rapidly to release the granular mass that spread into the horizontal channel until it came to rest, while the flow was recorded with the video camera at 50 frames per second. Finally, the movie was processed with MATLAB[®] in order to track the free surface and position of the front of the granular

TABLE II. Experimental setup for initial columns of experiments listed in Table I. h_1 and h_2 are the column height of small and large grains, respectively, and % of small grains $\equiv 100(h_o x_o)^{-1} \int_0^{h_o} \int_0^{x_o} (c_1/[c_1 + c_2])_{t=0} dx dy$.

| Sets | Experiment | h_1 | h_2 | Small grains (%) |
|-----------|------------|----------|----------|------------------|
| A1 and A2 | 1 | | h_o | 0 |
| | 2 | $1/3h_o$ | h_o | 11 |
| | 3 | $2/3h_o$ | h_o | 20 |
| | 4 | h_o | h_o | 27 |
| | 5 | h_o | $2/3h_o$ | 47 |
| | 6 | h_o | $1/3h_o$ | 70 |
| | 7 | h_o | | 100 |
| B1 and B2 | 1 | h_o | h_o | 25 |
| | 2 | h_o | h_o | 50 |
| | 3 | h_o | h_o | 75 |
| | 4 | h_o | h_o | 100 |

flow. This procedure was done for each column aspect ratio of the experiments described in Table II, so that each experiment was repeated five times.

As the effect of gate removal was not considered in the numerical simulations, we verified the time of opening and found that it was ~ 0.1 s, which was less than about 5% and 10% of the typical flow duration in water and air, respectively. Furthermore, the error in the front velocity was ± 0.05 m s $^{-1}$, which corresponded to less than about 4% and 8% of the typical flow front velocity in air and water, respectively.

B. Numerical solution

Governing equations were solved in a closed rectangular domain with the same horizontal dimensions as the experiments. As the pressure fields for each constituent were not known, following [13] we applied the implicit finite volume pressure-correction scheme proposed by Ref. [41] to each constituent, which is an iterative procedure for calculating the flow and pressure fields that is described in detail in Ref. [13].

Regarding the boundary conditions, the grid was arranged such that the wall coincided with a control volume face, thus requiring only specifying the flow across the wall as a boundary condition to the pressure-correction equation (pp. 129–130 of Ref. [41]), which was equal to zero since the domain was closed. Additionally, the no-slip boundary condition was considered for the fluid, so that the fluid velocity parallel to the walls was equal to zero. A zero momentum flux across the walls was assumed for the solid constituents, so that the gradient of the solids velocity parallel to the walls was equal to zero, which means that solid particles can slip along the walls. Finally, a wall friction equal to the inner Coulomb friction φ was assumed.

The solution algorithm for one time step can be summarized as follows. (i) Start the calculation of the fields at the new time step with the solution of the previous time step. (ii) Solve the discretized momentum equations for the fluid. (iii) Solve the discretized momentum equations for the small particles. (iv) Solve the discretized momentum equations for the large particles. (v) Solve the pressure-correction equation for the fluid, and correct fluid pressure and velocities (underrelaxed). (vi) Solve the pressure-correction equation for the small particles, and correct solid pressure and velocities (underrelaxed). (vii) Solve the pressure-correction equation for the large particles, and correct solid pressure and velocities (underrelaxed). (viii) Solve the discretized conservation of mass equation for the small particles. (ix) Solve the discretized conservation of mass equation for the large particles. (x) With the new fields, return to step (ii) until a converged solution for both the continuity and momentum equations is satisfied to an acceptable tolerance (difference in velocity between two successive iterations less than 1 mm s $^{-1}$) for each constituent.

We solved numerically the four sets of experiments presented in Table I. The horizontal dimension of the computational domain L was given by the experimental facility (i.e., $L = 1.5$ m); whereas the vertical dimension H was chosen as $H = 2h_o$, as we verified that for H larger than $\sim 1.5h_o$ the influence of the boundary condition at the top of the computational grid was negligible. For simplification and because the horizontal dimension of the domain was fixed, independent of the experiment, we used a fixed grid size of $\Delta x = \Delta y = 7.14 \times 10^{-3}$ m (i.e., $L/\Delta x = 210$), and a time step of $\Delta t = 2.5 \times 10^{-3}$ s (i.e., $\sqrt{Lg^{-1}}/\Delta t = 156$), such as $\Delta x/\Delta t = 2.9$ m s $^{-1}$ was about twice the maximum front propagation speed. The details of the numerical setup for each simulation are also summarized in Table I.

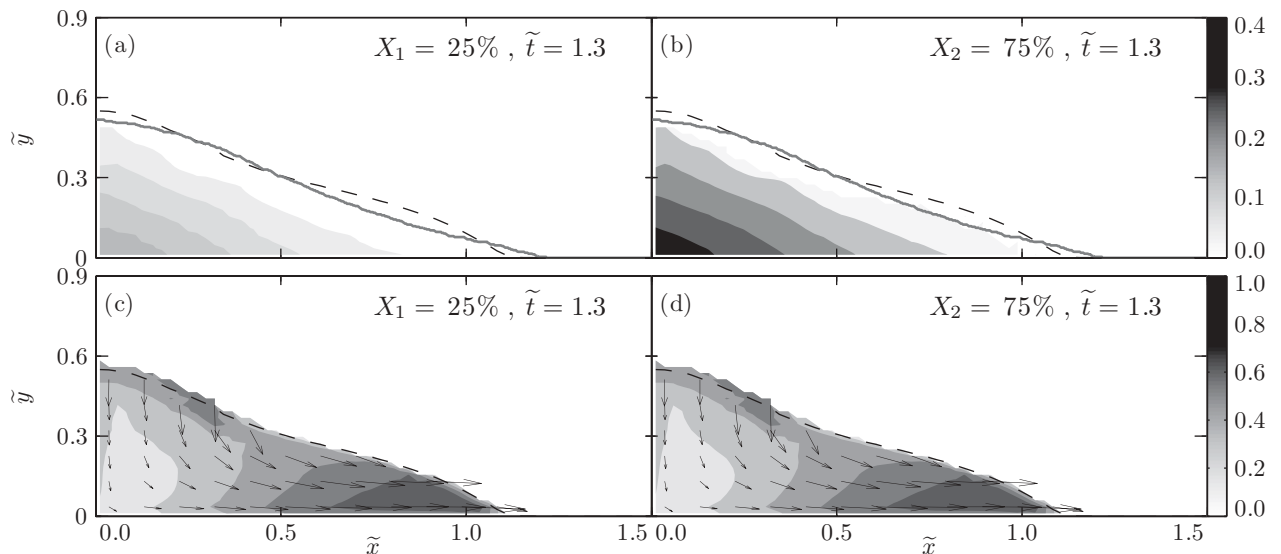


FIG. 3. Results of granular column collapse and spreading in air with grains size of 3 mm and columns with $h_o/x_o = 3$. Numerical experiments were carried out by varying the proportions of the same solid constituent between 25% and 75%. (a),(b) Contour graphs of the dimensionless solid pressures \tilde{p}_1 and \tilde{p}_2 , respectively, and experimental (—) and computed $c^{-1} \int_0^{\tilde{H}} [c_1(\tilde{x}, \tilde{y}) + c_2(\tilde{x}, \tilde{y})] d\tilde{y}$ (---) free surface of the granular flow. (c),(d) Spatial variation of the magnitude (contour) and direction (arrows) of the solid velocities \tilde{u}_1 and \tilde{u}_2 , respectively.

IV. RESULTS

A. Validation of the model equations

To validate the new constitutive relation (10) that describes the interactions between solid constituents in a dense regime, we first conducted numerical experiments for the collapse and spreading of a granular column composed by two solid species, named 1 and 2, with equal material density and diameter (i.e., $\gamma_1 = \gamma_2$ and $d_1 = d_2$) in air. In this condition, the three-phase flow dynamics is identical to the monodisperse counterpart (i.e., two-phase flows) validated by Ref. [13]. We also carried out these numerical experiments with the larger particles in air (experiment A1.1 of Table II), for which the fluid effects are less important [13], and we varied the relative solid fractions $X_\alpha = c_\alpha / (c_1 + c_2)$ between $(X_1, X_2) = (0\%, 100\%)$, $(25\%, 75\%)$, and $(50\%, 50\%)$. The results of this analysis are presented in Figs. 3 and 4 that also show a comparison with the experimental measurements. It is shown that the total solid pressure is partitioned according to the relative solid fraction of each component [Figs. 3(a) and 3(b)], and is equal to the simulated solid pressure of one solid constituent [Fig. 4(a)]. Furthermore, in the three-constituent simulations, both solid components have the same solid velocity [Figs. 3(c) and 3(d)]

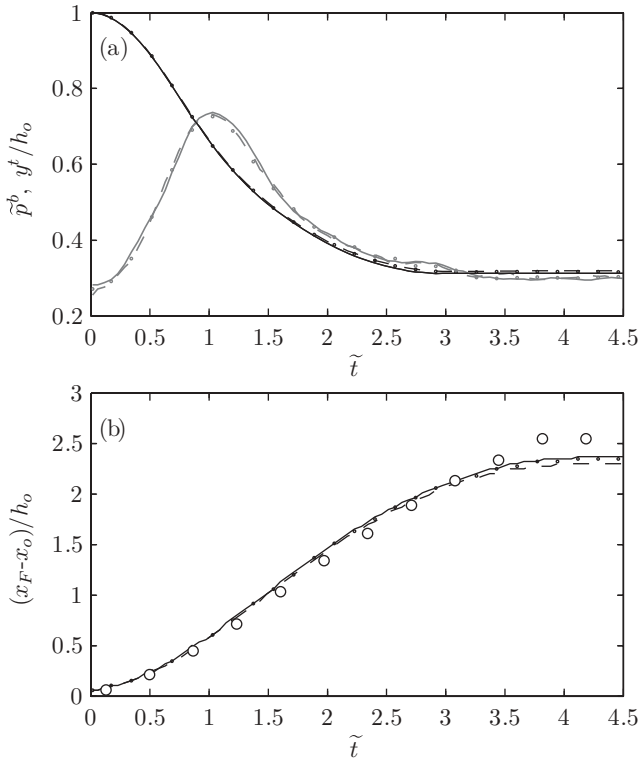


FIG. 4. Results of granular column collapse and spreading in air with grains size of 3 mm and columns with $h_o/x_o = 3$. The numerical experiments were carried out by varying the proportions of the same solid constituent between $(0\%, 100\%)$, $(25\%, 75\%)$, and $(50\%, 50\%)$. (a) Time series of the total solid pressure at the left bottom corner of the column $\tilde{p}^b = \tilde{p}_1^b + \tilde{p}_2^b$ (gray lines) and the column height at the left top y^t/h_o (black lines). (b) Comparison between measured (c) and simulated time series of the dimensionless front position $(x_F - x_o)/h_o$ for $(0\%, 100\%)$ (—), $(25\%, 75\%)$ (- · - ·), and $(50\%, 50\%)$ (---).

and front speed [Fig. 4(b)], thus preserving the mixture force balance independent of the fractions of the components, which validates the solid interaction closure (10), as the two solid constituents simulations give the same numerical results as for the case of a single constituent.

Note that Fig. 4(b) shows that during the deceleration stage at the end of the granular flow, the agreement between simulations and experiments is not as good as during earlier stages. This is because when the flow decelerates in experiments, some particles escape from the surface of the granular flow, which does not occur in simulations, thus leading to a larger runout distance in experiments than in numerical simulations. It is important to note that this difference between experiments and simulations does not exceed 10% of h_o .

Before validating the constitutive relation (10) for the case of binary mixtures of small and large grains, it is necessary to analyze the kinetic sieving coefficient $\sigma \geq 0$, introduced in the empirical function $\eta(\sigma)$ of Eq. (14) in order to address the kinetic sieving of small grains in the solid pressure closure (4).

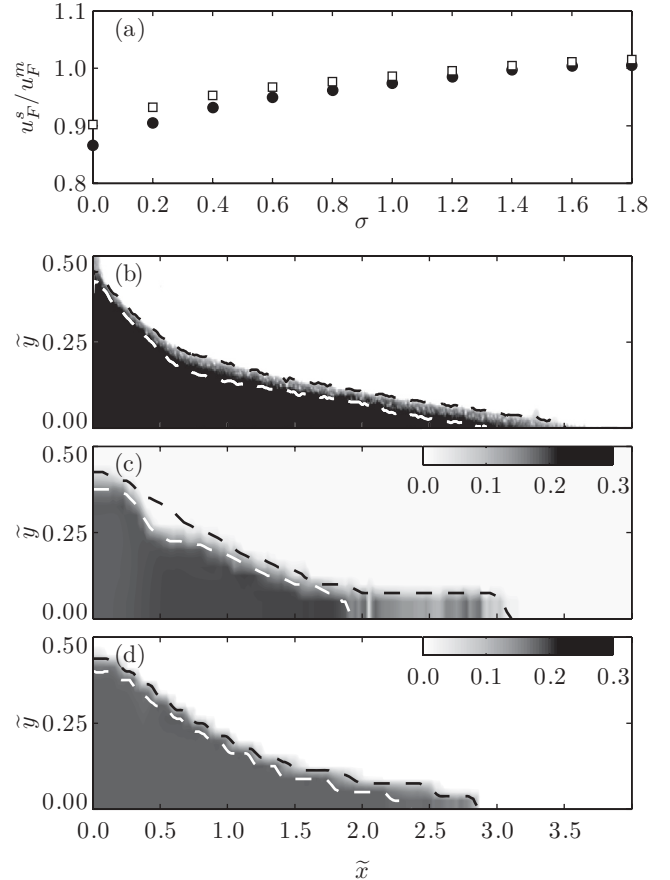


FIG. 5. (a) Ratio between simulated and measured front speed u_F^s/u_F^m , as a function of σ for experiments A1.4 (\bullet) and B1.1 (\square) of Table II and $h_o/x_o = 2$. (b) Image of the experimental deposit of A1.4. (c, d) Numerical results showing the contour graph of the solid concentration of small particles c_1 for simulated deposits of A1.4 with $\sigma = 1.4$ (c) and $\sigma = 0.0$ (d). White dashed line marks the separation between the layer with small and large grains at the bottom of the deposit and the layer rich in large grains at the surface (in where $c_1 < 0.1$), and the black dashed line represents the free surface of the deposit.

Following [13], the front speed in the constant velocity regime $u_F = \max(dx_F/dt)$, is used as a control parameter to compare the numerical results with the experimental measurements. We chose the front speed because we verified that it was the most sensitive parameter that allowed us to validate the theory.

A sensitivity analysis of the front speed depending on σ is presented in Fig. 5(a), which shows the ratio between simulated and measured front speed u_F^s/u_F^m , for experiments A1.4 and B1.1 of Table II. The simulated front speed is smaller than the experimental measurements when $\sigma = 0$, but approaches those measurements when σ increases [Fig. 5(a)]. The final deposit morphology is also fairly well simulated when increasing σ [compare Figs. 5(c) and 5(d) with Fig. 5(b)], although the fit of the deposit morphology is not as good as in the case of only one solid species [see comparison between measured and simulated free surface of the granular flow in Figs. 3(a) and 3(b)].

The influence of σ can be explained by the expansion of the granular network induced by particle segregation. This is shown in Figs. 5(b)–5(d) by comparing the measured [Fig. 5(b)] and simulated deposits of A1.4 in cases of $\sigma = 1.4$ [Fig. 5(c)] and $\sigma = 0.0$ [Fig. 5(d)]. Percolation of the small grains induces the segregation of the large particles at the top of the flow [Figs. 5(b) and 5(c)], which in turn decreases the mixture concentration. This is because in the cases analyzed here, the relative concentration of small grains is close to 28%, which corresponds to the optimal packing (see Fig. 1) so that any change in the relative concentration of small grains (increase or decrease) produces a decrease in the loose packing mixture concentration, thus increasing the mixture

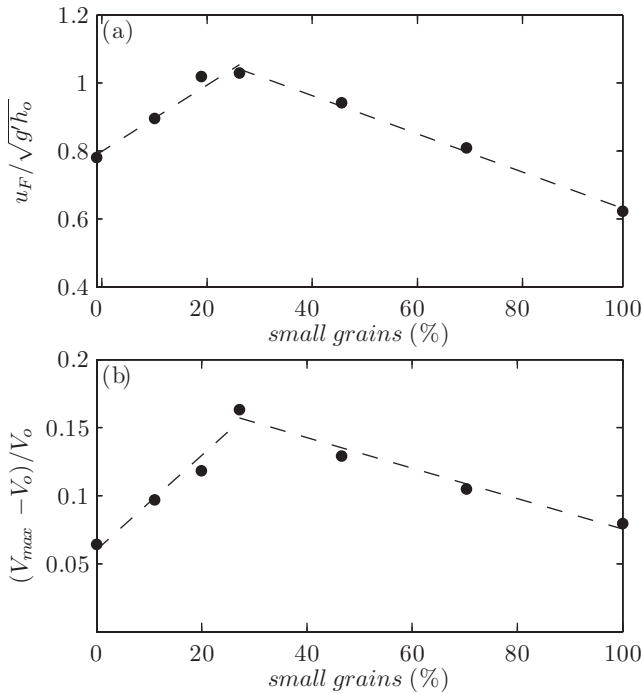


FIG. 6. Experimental results for experiments A1.4 ($d_1/d_2 = 0.067$ in air) and $h_o/x_o = 2$. (a) Dimensionless front speed, $u_F/\sqrt{g h_o}$, and (b) maximum increase of mixture volume $(V_{max} - V_o)/V_o$, as a function of the initial relative concentration of small grains. The experimental tendency is represented by the dashed line.

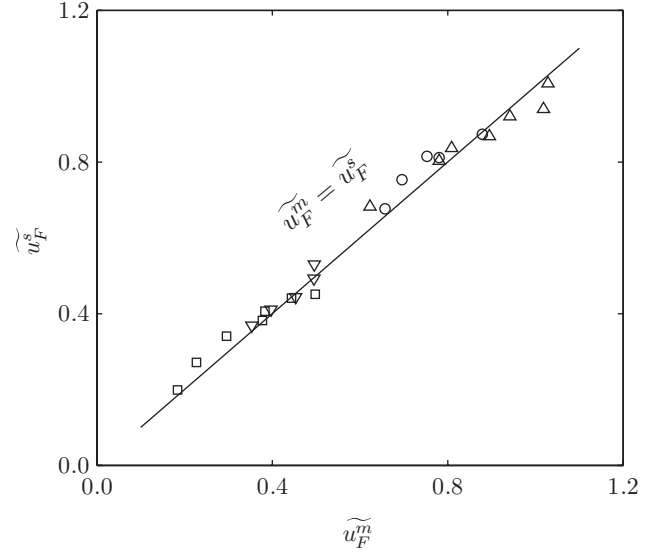


FIG. 7. Simulated, \tilde{u}_F^s , versus modelled, \tilde{u}_F^m , dimensionless front speed for the four sets of experiments of Table I with $h_o/x_o = 3$ and $\sigma = 1.4$.

volume. This volumetric expansion is then reflected in the front speed as the kinetic energy is proportional to both the solid concentration and square velocity, so that by conservation of energy a decrease in solid concentration is compensated with an increase in speed. Experimental measurements in air are

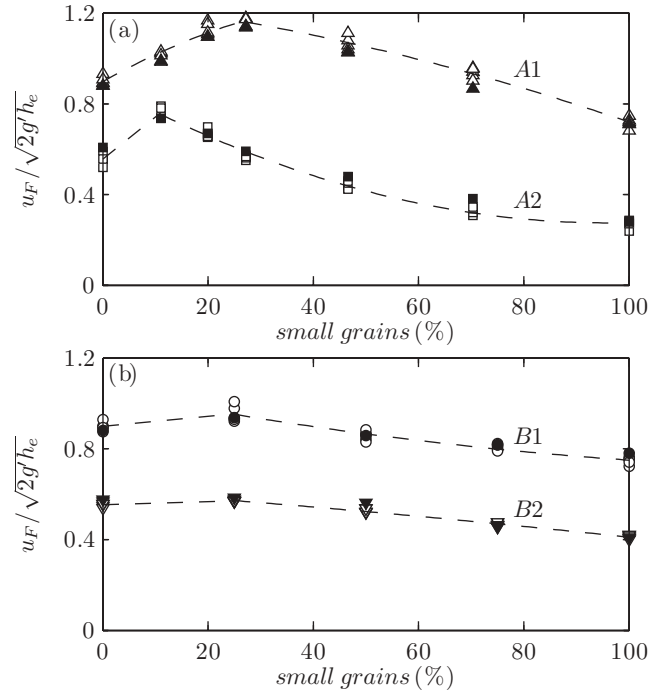


FIG. 8. Froude number $Fr = u_F/\sqrt{2g h_e}$ as a function of the initial volume fraction of small grains for sets A1 (in air, Δ) and A2 (in water, \square) (a), and B1 (in air, \circ) and B2 (in water, ∇) (b) of Table I. White marks are experimental measurements with $h_o/x_o = \{2,3,4,6,8\}$; and black marks are simulation results with $h_o/x_o = 6$ and $\sigma = 1.4$. The experimental tendency is represented by the dashed line.

used to test this hypothesis, and the main results are shown in Fig. 6 that presents the dimensionless front speed $u_F/\sqrt{g'h_o}$ and the maximum increase of mixture volume $(V_{\max} - V_o)/V_o$ as a function of the initial relative concentration of small grains, with $V_o = x_o h_o$ and $V_{\max} = \max[\int_0^L h_s(x,t)dx]$ where h_s is the experimental free surface of the granular flow. The experimental results show that when the initial volume fraction of small grains increases until $\sim 28\%$, both the front speed and the mixture volume increase.

The results described above can be explained in terms of the governing equations. In particular, the segregation of small and large grains that explains the increase in front speed in Fig. 5(a) is modulated by σ , explained as follows. When σ increases, the empirical function $\eta(\sigma)$ of Eq. (14) decreases, so that accordingly with Eqs. (4) and (13), there is an interval of the mixture concentration ($\eta c^* < c_1 + c_2 < c^*$) for which the solid pressure of large grains exists and the solid pressure of small grains is set to zero. Once the solid pressure of small grains is set to zero, the force balance is broken and the small grains fall down, thus generating percolation and the resulting segregation of the granular flow. Moreover, as a consequence of segregation, there is an expansion of the flow because of the decrease in mixture concentration [see (11) and Fig. 1, which

shows that when the proportion of small grains increases above 28%, the mixture concentration decreases], which produces the increase in front speed that is observed in the experimental measurements of Fig. 6 and in the simulation results. It is argued that this increase in flow speed may be explained in terms of the kinetic energy of the flow, which is proportional to both the solid concentration and the square of the flow velocity, so that a decrease in solid concentration is compensated by an increase in speed. In contrary, when σ approaches 0, $\eta(\sigma)$ is closer to 1, so that there is no practical difference between large and small grains in terms of solid pressure. Hence, there is neither segregation nor expansion of the granular flow, and consequently the front speed stays invariant with respect to the situation described by a homogeneous granular flow.

Using $\sigma = 1.4$ in Eq. (14), for which $u_F^s/u_F^m \approx 1$, to model the kinetic sieving of small grains, the four sets of experiments summarized in Table I were simulated and the results for $h_o/x_o = 3$ are presented in Fig. 7. A good agreement between simulated and measured front speed is observed, thus validating the system of governing equations for dense granular flows of binary mixtures of small and large spherical particles of equal mass density in an ambient fluid.

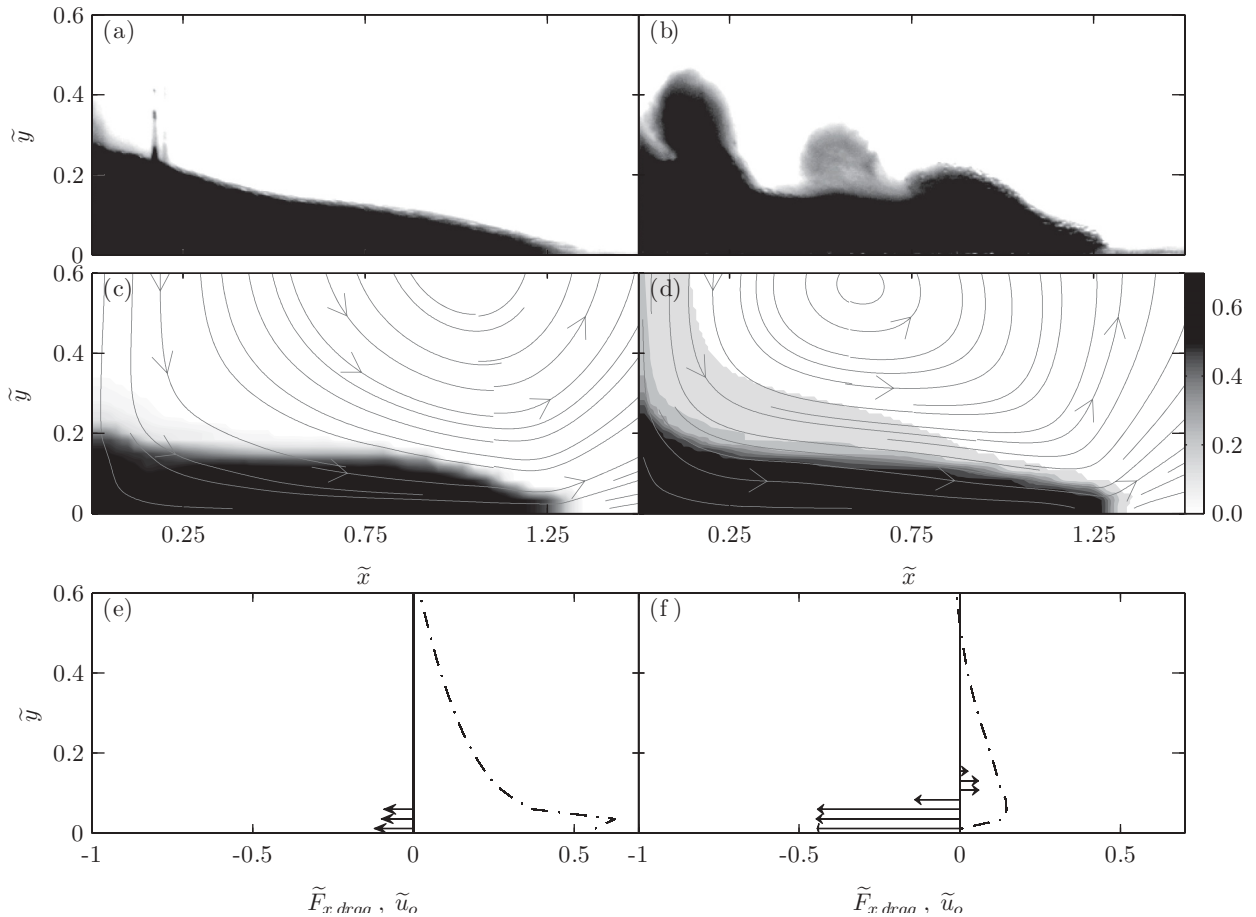


FIG. 9. Results for experiments A1.4 at $\tilde{t} = 1.9$ (in air, left panels) and A2.4 at $\tilde{t} = 3.1$ (in water, right panels). (a),(b) Experimental image. (c),(d) Contour graph of the total solid concentration, $c_1 + c_2$, and the streamlines of fluid velocity (\rightarrow). (e),(f) Dimensionless horizontal fluid velocity, \tilde{u}_o ($- \cdot - \cdot$), and drag force, $\tilde{F}_{x,drag}$ (\rightarrow), profiles in the front area.

B. On the dynamics of three-phase dense granular flows

In order to verify that the results obtained from experiments are independent of the initial column aspect ratio, we repeated each set of experiments with columns of $h_o/x_o = \{2, 3, 4, 6, 8\}$. For comparison of the results, we used the equivalent height $h_e = h_e(\tan \varphi, h_o/x_o)$, introduced by Ref. [13] to subtract the effects of $\tan \varphi$ and h_o/x_o , which for the case of monosized glass beads ($\varphi = 26^\circ$) is

$$\frac{h_e}{h_o} = \begin{cases} 0.4 & 1 \leq h_o/x_o \leq 3, \\ 0.76(h_o/x_o)^{-0.58} & 3 < h_o/x_o \leq 16, \end{cases} \quad (16)$$

such that the front speed can be written generically as

$$u_F = \text{Fr} \sqrt{2g'h_e}, \quad (17)$$

where Fr is a Froude number that is independent of $\tan \varphi$ and h_o/x_o , so that the dimensionless front speed or Froude number $\text{Fr} = u_F / \sqrt{2g'h_e}$ collapses to a single value when considering the same conditions of ambient fluid and solids mixture but different column aspect ratio.

Figure 8 shows Fr as a function of the initial volume fraction of small grains for the four sets of experiments of Table I. For the case of experiments in air (experiments A1 and B1 in Fig. 8), the front speed increases when the initial volume fraction of small grains increases until $\sim 28\%$ (Fig. 8), which according to Eq. (11) corresponds to the optimal or maximum packing concentration of the mixture (see Fig. 1). As discussed in the previous section, this behavior could be caused by particle segregation that increases the solid mixture volume, and it is more important for binary mixtures with $d_1/d_2 = 0.067 < 0.15$ [experiments A1 in Fig. 8(a)] than for binary mixtures with $d_1/d_2 = 0.233$ [experiments B1 in Fig. 8(b)]. When repeating the same experiments in water, the increase in front speed due to particle segregation is damped, and the maximum value of the front speed is shifted toward smaller relative concentration of small grains [see experiments A2 in Fig. 8(a)]. This behavior can be attributed to the nature of the ambient fluid, and can be explained by the competition between particle segregation and ambient fluid effects. In fact, the front speed decreases when the particle diameter decreases, and this effect is enhanced in water [13].

The effect of the ambient fluid is illustrated in Fig. 9 that presents a comparison of the results for experiments in air and in water. Although in both cases drag forces coupled with wall fluid viscous effects counteract the movement of the solids [see Figs. 9(e) and 9(f) and discussion in Ref. [13]], the ambient fluid effects are more important in water than in air. Furthermore, Figs. 9(a)–9(d) show that, in general, there is a good agreement between the experimental and numerical morphologies of the granular flow. Apparent discrepancies are observed, however, in the case of ambient water for which experiments show that suspended particles at the top of the granular flow are concentrated in eddies [Fig. 9(b)], whereas numerical simulations reveal a smooth region with low concentration of particles [Fig. 9(d)]. This is because the experimental image corresponds to just one realization and the results of the model equations correspond to an average over many realizations. In fact, by using the equivalent height h_e described in Eq. (17) to scale the images of experiments A2.4 of Table II with the same dimensionless time $t\sqrt{2g'/h_e}$,

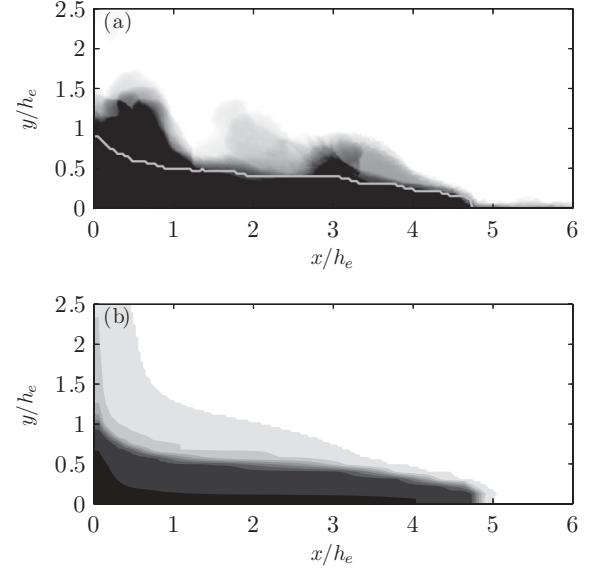


FIG. 10. (a) Experimental average image of experiments A2.4 at $t\sqrt{2g'/h_e} = 8.5$. The gray solid line delimits the simulated area with $c_1 + c_2 \geq 0.6$. (b) Simulated contour graph of the total solid concentration of experiment A2.4 and $h_o/x_o = 6$ at $t\sqrt{2g'/h_e} = 8.5$.

a better fit is observed in terms of the flow morphology as shown in Fig. 10. This figure shows that after averaging the experimental images, the eddies associated to the suspended particles at the top of the flow are also averaged, thus leading to the same smooth region as in the simulations. Also, this figure validates the use of h_e as scaling parameter when using different h_o/x_o , because not only the front speed (Fig. 8) but also the flow morphology collapses to a single value when considering the same conditions of ambient fluid and solids mixture but different h_o/x_o .

V. DISCUSSION AND CONCLUSIONS

The coupled dynamics of the constituents of a dense granular flow composed of a binary mixture of small and large grains and immersed in an ambient fluid was studied. For doing this, we extended the two-phase approach proposed by Ref. [13] to the case of flowing dense binary mixtures of solid particles by including in the momentum equations a constitutive relation that describes the interaction mechanisms between the solid constituents in a dense regime. This theory was validated by comparing the numerical results with experimental measurements of flows resulting from the collapse, in ambient air or water, of two-dimensional granular columns that consisted of mixtures of small and large spherical particles of equal mass density.

Our results suggest that the model equations include the essential features that describe the dynamics of dense granular flows of mixtures of small and large spherical particles of equal mass density and surface roughness (Fig. 7). The key feature of the model equations is the new constitutive relation (10), which correctly represents the interactions between the solid species in a dense regime, since one species can be split into several subconstituents and the resulting dynamics is independent of

that subdivision (see Figs. 3 and 4). With this new constitutive relation, the effect of difference in diameter between the two solid constituents is only taken into account in the model through the interactions with the ambient fluid. However, the dynamics of these binary mixtures is incompletely accounted for unless the kinetic sieving of small grains is included (Fig. 5). For doing this, the empirical function $\eta(\sigma)$ of Eq. (14) was introduced to represent the fact that under a critical value of the mixture concentration, only the small particles fall down while the large particles remain packed [5]. The direct effect of Eq. (14) in the solid pressure closure (4) was the segregation of the constituents [compare Figs. 5(c) and 5(d)], which can be explained by the squeeze expulsion mechanism, proposed first in Ref. [5] and later by Refs. [14,24], for which percolation of small grains produces force imbalances at the base of the flow and forces the large particles to move upward. This mechanism was a natural result of the model equations.

An important consequence of the segregation in the granular flow is the increase of the volume of the binary mixture because of the decrease of the mixture concentration, which is then reflected in an increase of the front speed (see Fig. 5). This is because in the cases analyzed here, the relative concentration of small grains is close to 28%, which corresponds to the optimal packing (see Fig. 1), so that any change of the spatial variation of the relative concentration of small grains (increase or decrease) produces a decrease in the loose packing mixture concentration, thus increasing the mixture volume. This volumetric expansion is then reflected in the front speed as the kinetic energy of the flow is proportional to both the solid concentration and the square of the flow velocity, so that a decrease in solid concentration is compensated by an increase in speed. The increase in flow mobility for binary mixtures having small amounts of small grains has been reported in experiments [18,19] and in soft particle discrete element numerical simulations [20]. In these studies, the mobility increase was attributed to a thin layer of small particles that may change the frictional dynamics at the base of the flow [19,20]. However, the results of Fig. 5 suggest that the increase in flow speed caused by the volumetric expansion of the flow related to the particle segregation can also explain the enhanced mobility. This relation between mobility and segregation may be in contradiction with Ref. [19] who found that a deposit of a granular flow with high mobility appears to have less segregation than a deposit of a flow with low mobility. However, our results agree with that of Refs. [18–20] as the maximum flow mobility occurs for mixture concentrations close to the maximum packing concentration ($\sim 28\%$ of fraction of small grains; see curves A1 and B1 of Fig. 8), for which the increase in volume due to segregation is greater [see Eq. (11) and Fig. 1]. Hence, the increase in flow front speed and mobility may be the result of both the expansion of the granular mixture and the lubrication at the base of the flow, although other effects could also contribute to the increase in front speed. For instance, chaos was introduced into our system A as particles could not return to their near-perfect initial state, whereas the initial state of our system B was closer to a natural system in terms of initial preparation. Further experimental analysis is required to elucidate this issue. These results, however, show the necessity of considering

small and large grains in the analyses of granular flows in nature.

Regarding the ambient fluid effects, [13] showed that in the context of dense granular flows, the main forces that describe the interactions between fluid and solid particles are the hydrodynamic fluid pressure (or pore pressure) and the drag forces. This is because hydrodynamic fluid pressure can hold the reduced weight of the solids, thus inducing a transition from dense-compacted to dense-suspended granular flows, whereas drag forces counteract the solids movement, especially within the near-wall viscous layer. Also, [13] showed that fluid turbulence is particularly important and has to be considered in the analysis. This is explained by the fact that fluid turbulence contributes to the solid-phase force balance, as fluid turbulence decreases the fluid velocity, thus increasing drag forces that finally counteract the gravity in the solid-phase force balance. As a consequence, small grains are more resistant to flow than large grains, so that the front speed decreases when the grain size decreases, and this behavior is more pronounced in water than in air. In the case of the three-constituent granular flow analyzed here, these ambient fluid effects help to explain the results of Fig. 8, which shows that the increase in flow speed due to the volumetric expansion is damped in water compared to the case in air [compare experiments A1 and A2 of Fig. 8(a)]. As shown in Figs. 9(e) and 9(f), this occurs because the drag forces coupled with the wall fluid viscous effects counteract the movement of the solid particles. Therefore, although a mixture of small and large grains may segregate and the front speed may increase, fluid drag forces can counteract the movement of the solids, thus competing with segregation.

ACKNOWLEDGMENTS

The first author acknowledges financial support from a CONICYT doctoral fellowship (Chile) and the complement granted by the project ECOS-CONICYT C06U01 (France-Chile). The first author also thanks the office facilities at Centre for Water Research, The University of Western Australia. We thank Alberto de la Fuente, Yarko Niño, and Kraig Winters for their helpful comments on an earlier draft.

APPENDIX: DERIVATION OF THE MATHEMATICAL REPRESENTATION OF THE CONSTITUTIVE RELATION BETWEEN SOLID CONSTITUENTS IN A DENSE REGIME

For obtaining the constitutive relation that represents the interaction force between the solid components in a dense regime $\hat{m}_{\beta\alpha i} = -\hat{m}_{\alpha\beta i}$, we follow the second guiding principle proposed by Ref. [22] to describe the motion of a constituent. This principle states that we may, in abstraction, isolate a constituent from the rest of the mixture as long as the effects of the other components are considered as forces acting upon it. In this context, let us do the abstraction of a volume V_α , containing only particles of the solid constituent α and surrounded by a mixture that contains all the other components [Fig. 11(a)]. This abstraction allows us to interpret the action of the other solid component β on the constituent α as superficial forces

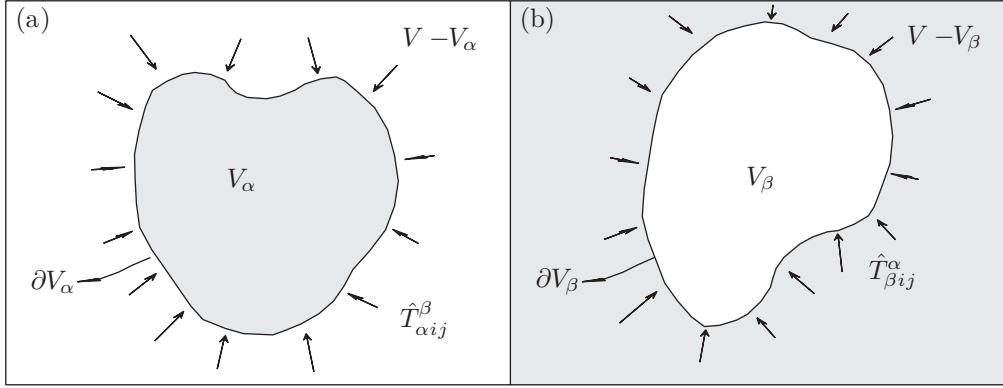


FIG. 11. In abstraction the solid constituents α and β are isolated from the rest of the mixture. (a) $\int_{\partial V_\alpha} \hat{T}_{\alpha ij}^\beta n_j dS$ corresponds to the action force of the solid constituent β acting on the surface ∂V_α of V_α , and in response there is an equivalent and opposite force acting on β , $-\int_{\partial V_\alpha} \hat{T}_{\alpha ij}^\beta n_j dS$. (b) In the same way, $\int_{\partial V_\beta} \hat{T}_{\beta ij}^\alpha n_j dS$ corresponds to the action force of the solid constituent α acting on the surface ∂V_β of V_β , and in response there is an equivalent and opposite force acting on α , $-\int_{\partial V_\beta} \hat{T}_{\beta ij}^\alpha n_j dS$. Thus, the mutual actions between constituents are represented by $\int_V \hat{m}_{\beta\alpha i} dV = -\int_V \hat{m}_{\alpha\beta i} dV = \int_{\partial V_\alpha} \hat{T}_{\alpha ij}^\beta n_j dS - \int_{\partial V_\beta} \hat{T}_{\beta ij}^\alpha n_j dS$.

acting on the surface ∂V_α of V_α , such that this action can be represented by a tensor of superficial forces $\hat{T}_{\alpha ij}^\beta$ acting on ∂V_α . In this way, the action force of the constituent β on α is $\int_{\partial V_\alpha} \hat{T}_{\alpha ij}^\beta n_j dS$, with n_j the outward normal vector, and in response there is an equivalent and opposite force acting on β , $-\int_{\partial V_\alpha} \hat{T}_{\alpha ij}^\beta n_j dS$. Similarly, if we now consider the same abstraction for the constituent β [Fig. 11(b)], then the action force of the solid constituent α on β is $\int_{\partial V_\beta} \hat{T}_{\beta ij}^\alpha n_j dS$, and in response there is an equivalent and opposite force acting on α , $-\int_{\partial V_\beta} \hat{T}_{\beta ij}^\alpha n_j dS$.

Thus, the reciprocal interaction force between the solid constituents α and β has two components, one representing the action force of the constituent β on α that is applied on the border ∂V_α , and another representing the reaction force of the constituent β on α that is applied on the border ∂V_β , such that

the reciprocal force is represented by

$$\begin{aligned} \int_V \hat{m}_{\beta\alpha i} dV &= -\int_V \hat{m}_{\alpha\beta i} dV \\ &= \int_{\partial V_\alpha} \hat{T}_{\alpha ij}^\beta n_j dS - \int_{\partial V_\beta} \hat{T}_{\beta ij}^\alpha n_j dS. \end{aligned} \quad (A1)$$

Applying the divergence theorem and since $dV_\alpha = c_\alpha dV$, so that

$$\int_{\partial V_\alpha} \hat{T}_{\alpha ij}^\beta n_j dS = \int_{V_\alpha} \frac{\partial \hat{T}_{\alpha ij}^\beta}{\partial x_j} dV_\alpha = \int_V c_\alpha \frac{\partial \hat{T}_{\alpha ij}^\beta}{\partial x_j} dV, \quad (A2)$$

(A1) is then written as

$$\hat{m}_{\beta\alpha i} = -\hat{m}_{\alpha\beta i} = c_\alpha \frac{\partial \hat{T}_{\alpha ij}^\beta}{\partial x_j} - c_\beta \frac{\partial \hat{T}_{\beta ij}^\alpha}{\partial x_j}. \quad (A3)$$

-
- [1] C. Ancey, *J. Non-Newtonian Fluid Mech.* **142**, 4 (2007).
[2] J. Ottino and D. Khakhar, *Annu. Rev. Fluid Mech.* **32**, 55 (2000).
[3] B. Zanuttigh and A. Lamberti, *Rev. Geophys.* **45**, RG3006 (2007).
[4] C. Campbell, *Powder Technol.* **162**, 208 (2006).
[5] S. B. Savage and C. K. K. Lun, *J. Fluid Mech.* **189**, 311 (1988).
[6] T. Takahashi, *Debris Flow* (IAHR Monograph, A.A. Balkema Publishers, Rotterdam, 1991).
[7] V. Dolgunin and A. Ukolov, *Powder Technol.* **83**, 95 (1995).
[8] J. M. N. T. Gray and V. A. Chugunov, *J. Fluid Mech.* **569**, 365 (2006).
[9] B. Zanuttigh and P. Ghilardi, *J. Hydrology* **391**, 175 (2010).
[10] N. Thomas, *Phys. Rev. E* **62**, 961 (2000).
[11] O. Pouliquen, J. Delour, and S. B. Savage, *Nature (London)* **386**, 816 (1997).
[12] H. A. Makse, S. Havlin, P. R. King, and E. Stanley, *Nature (London)* **386**, 379 (1997).
[13] C. Meruane, A. Tamburrino, and O. Roche, *J. Fluid Mech.* **648**, 381 (2010).
[14] O. Pouliquen and J. Vallance, *Chaos* **9**, 621 (1999).
[15] J. Vallance and S. B. Savage, in *IUTAM Symposium on Segregation in Granular Materials*, edited by A. Rosato and D. Blackmore (Kluwer Academic, Dordrecht, The Netherlands, 2000), pp. 31–51.
[16] N. Burtally, P. J. King, and M. R. Swift, *Science* **295**, 1877 (2002).
[17] P. Biswas, P. Sanchez, M. R. Swift, and P. J. King, *Phys. Rev. E* **68**, 050301 (2003).
[18] O. Roche, M. Gilbertson, J. Phillips, and R. Sparks, *Earth Planet. Sci. Lett.* **240**, 401 (2005).
[19] J. Phillips, A. Hogg, R. Kerswell, and N. Thomas, *Earth Planet. Sci. Lett.* **246**, 466 (2006).
[20] E. Linares-Guerrero, C. Goujon, and R. Zenit, *J. Fluid Mech.* **593**, 475 (2007).
[21] L. Staron and E. Lajeunesse, *Geophys. Res. Lett.* **36**, L12402 (2009).
[22] C. Truesdell, *Rand. Lincei* **22**, 33 (1957).
[23] C. Truesdell, *Rational Thermodynamics* (Springer-Verlag, Berlin, 1984).

- [24] J. Gray and A. Thornton, *Proc. R. Soc. A* **461**, 1447 (2005).
- [25] A. Thornton, J. Gray, and A. Hogg, *J. Fluid Mech.* **550**, 1 (2006).
- [26] J. M. N. T. Gray and C. Ancey, *J. Fluid Mech.* **629**, 387 (2009).
- [27] R. Di Felice, *Chem. Eng. Sci.* **50**, 1213 (1995).
- [28] W. Rodi, *Turbulence Models and Their Application in Q Hydraulics—A State-of-the-Art Review* (IAHR Monograph, A.A. Balkema Publishers, Delft, 1983).
- [29] C. Crowe, R. Troutt, and J. Chung, *Annu. Rev. Fluid. Mech.* **28**, 11 (1996).
- [30] C. Campbell, *Annu. Rev. Fluid Mech.* **22**, 57 (1990).
- [31] I. Goldhirsch, *Annu. Rev. Fluid Mech.* **35**, 267 (2003).
- [32] M. Goodman and S. Cowin, *J. Fluid Mech.* **45**, 321 (1971).
- [33] O. Pouliquen and Y. Forterre, *J. Fluid Mech.* **453**, 133 (2002).
- [34] J. Gray, C. Tai, and S. Noelle, *J. Fluid Mech.* **23**, 161 (2003).
- [35] E. Larrieu, L. Staron, and E. Hinch, *J. Fluid Mech.* **554**, 259 (2006).
- [36] Y. Forterre and O. Pouliquen, *Annu. Rev. Fluid Mech.* **40**, 1 (2008).
- [37] R. German, *Particle Packing Characteristics* (Metal Powder Industries Federation, Princeton, NJ, 1989).
- [38] R. Fedors and R. Landel, *Powder Technol.* **23**, 225 (1979).
- [39] R. Rutgers, *Nature (London)* **193**, 465 (1962).
- [40] I. Ippolito, L. Samsom, S. Bourles, and J. Hulin, *Eur. Phys. J. E* **3**, 227 (2000).
- [41] S. Patankar, *Numerical Heat Transfer and Fluid Flow* (Hemisphere, Taylor and Francis, New York, 1980).